PAPER

The effects of dopant concentration and excitation intensity on the upconversion and downconversion emission processes of β-NaYF₄:Yb³⁺,Er³⁺ nanoparticles†

Vivian Torres Vera, [ID] [a] Diego Mendez-Gonzalez, [ID] [aef] Diego J. Ramos-Ramos, [ID] [bc]
Asmae Igalla,[b] Marco Laurenti, [ID] [ade] Rafael Contreras-Caceres, [ID] [a]
Enrique Lopez-Cabarcos, [ID] [a] Elena Díaz, [ID] [c] Jorge Rubio-Retama,[ae]
Sonia Melle [ID] [b] and Oscar G. Calderón [ID] *[b]

The dopant concentration of lanthanide ions in photon upconversion nanoparticles (UCNPs) remains one of the key points to boost the brightness of these nanomaterials and, therefore, their application developments. Here, we analyzed the effect of Er³⁺ and Yb³⁺ dopant concentrations of β-NaYF₄:Yb³⁺,Er³⁺ nanoparticles on the visible upconversion and near-infrared downconversion luminescence intensities. Our approach carefully excluded all other factors whose variation affects luminescence properties such as the size, morphology, crystal structure, ion distribution, ligand, and surrounding medium, allowing us to exactly infer the influence of the ratio of Yb³⁺ to Er³⁺ ions on the nanoparticle luminescence. To maintain the size and morphological properties of nanoparticles, we used a total dopant concentration of 22% while varying the ratio of Yb³⁺ to Er³⁺ ions from 0 to 10. A huge increase in luminescence takes place as the Yb/Er ratio increases following a power-law behavior, and this luminescence enhancement is greater at low excitation intensities. Above a Yb/Er ratio of around two, saturation occurs with a slight peak when this ratio is around four. Simulations using a rate equation model showed that upconversion luminescence (UCL) is mainly produced by the energy transfer between neighboring Er³⁺ ions at low Yb/Er ratios, while at high ratios, the energy transfer from Yb³⁺ to Er³⁺ ions dominates. However, downconversion luminescence (DCL) is produced at all analyzed ratios, except 0, by the previous mechanism.

[a] *Department of Chemistry in Pharmaceutical Sciences, Complutense University of Madrid, E-28040 Madrid, Spain*

[b] *Department of Optics, Complutense University of Madrid, E-28037 Madrid, Spain. E-mail: oscargc@ucm.es*

[c] *GISC, Department of Materials Physics, Complutense University of Madrid, E-28040 Madrid, Spain*

[d] *Instituto de Ciencia de Materiales de Madrid, c/Sor Juana Inés de la Cruz, Cantoblanco, E-28049, Madrid, Spain*

[e] *Nanobiology Group, Instituto Ramón y Cajal de Investigación Sanitaria, IRYCIS, E-28034, Madrid, Spain*

[f] *Nanomaterials for Bioimaging Group, Departamento de Física de Materiales, Universidad Autónoma de Madrid, E-28049, Madrid, Spain*

† Electronic supplementary information (ESI) available: EDS measurements: estimation of Yb³⁺/Er³⁺ dopant ratios; XRD measurements: crystalline phase for UCNPS with different Yb³⁺/Er³⁺ ratios; TEM images showing nanoparticle size histograms for UCNPs with different Yb³⁺/Er³⁺ ratios; parameter values used in the theoretical model; derivation of the analytical expression for the population of the excited states in the low excitation signal regime. See DOI: 10.1039/d1tc01419f

1 Introduction

Nanocrystals doped with trivalent rare-earth ions are fascinating photoluminescent probes due to their attractive ability to produce photon upconversion without the need for expensive high-intensity excitation lasers such as those required for two-photon absorption or second harmonic generation.[1–3] Besides, rare-earth nanoparticles show large Stokes shifts, lack of photo-bleaching, absence of blinking, long fluorescent lifetimes, sharp emission bandwidths, and emission tuning capacity, which make them very attractive materials for a variety of applications such as optical imaging probes,[4] biolabeling,[5] sensing,[6] anti-counterfeiting,[7] solar cells,[8] small drug delivery systems,[9] or nanothermometry,[10] proving their tremendous scientific and technological potential.

Among the different photon upconversion mechanisms in lanthanide ions such as excited-state absorption (ESA), cooperative sensitization upconversion (CSU), cross-relaxation upconversion (CRU), or energy transfer upconversion (ETU), the latter is, by far, the most efficient one.[11,12] The ETU process requires two types of

8902 | *J. Mater. Chem. C*, 2021, **9**, 8902–8911

This journal is © The Royal Society of Chemistry 2021

ions namely sensitizers and activators, inserted into a low-phonon energy matrix. Sensitizer ions, typically Nd^{3+} or Yb^{3+} ions, absorb the excitation photons and transfer the energy to activator ions. The most common activator ions are Er^{3+}, Tm^{3+}, or Ho^{3+}, and they are characterized by exhibiting ladder-like arranged energy levels, which are essential to facilitate the successive energy-transfer steps that populate higher energy levels and, upon relaxation, release upconverted photons.[13] One of the most studied systems is based on $NaYF_4$:Yb^{3+},Er^{3+} nanoparticles due to their high upconversion efficiency which, among other factors, is related to the low phonon energy of the host matrix (around 360 cm^{-1}).[14] After excitation with a continuous wave (CW) laser at 980 nm, these nanoparticles exhibit three prominent upconversion bands located at the blue (410 nm), green (520 and 540 nm), and red (650 nm) wavelengths. Their intensities are very sensitive to variations in the surface area-to-volume ratio,[15] crystal structure,[16] lanthanide doping concentration[17] as well as the ligand and surrounding medium.[18–20] All these factors define the luminescence efficiency of upconversion nanoparticles (UCNPs). For this reason, understanding the role of these factors in the whole process will be desirable for the rational design of high luminescent UCNPs.

One of the most important factors affecting the luminescence efficiency is lanthanide doping concentrations. The optimal dopant concentrations of 2% Er^{3+} and 18% Yb^{3+} have been reported by Güdel et al. in order to obtain the most efficient near-infrared (NIR) to green upconversion in $NaYF_4$ microcrystals.[14,21,22] In the case of single-core nanoparticles, several studies have evaluated the influence of Er^{3+} and Yb^{3+} concentrations on luminescence properties. In general, an optimal Yb^{3+} concentration between 17 and 20% is assumed while the Er^{3+} concentration is kept relatively low (around 2–4%) to guarantee the distance between dopants and thus to minimize the energy loss resulting from cross-relaxation.[23–26] For example, Wang et al.[23] found that the green fluorescence lifetime of $NaYF_4$:Yb/Er nanoparticles increases when the Er^{3+} concentration decreases from 32% down to 0.5% while keeping the Yb^{3+} concentration constant at 20%. Cao et al.[25] studied powder samples of $NaYF_4$ doped with 2% of Er^{3+} and a wide range of Yb^{3+} co-doping concentrations, and found that the strongest visible emission occurs at 20% of Yb^{3+} since a greater increase in the Yb^{3+} concentration induces a transition from the hexagonal to the cubic phase, thus decreasing fluorescence emission. Other work by Kaiser et al.[26] found a maximum particle brightness for UCNPs doped with 14% of Yb^{3+} and 3% of Er^{3+} at low excitation intensities. Recently, the influence of the doping concentration on the green/red emission ratio was studied finding that an increase of Yb^{3+} content from 2 to 25 mol% induced tunable emission from green to red, being the highest red/green ratio achieved for 1% Er^{3+} and 20% Yb^{3+}.[27] On the other hand, core/shell structured UCNPs have also shown the ability to enhance their upconversion luminescence by increasing the Yb^{3+} doping level to very high values.[28,29]

Not only UCNPs show upconversion luminescence (UCL), but they also have even more efficient downconversion luminescence (DCL) in the near-infrared (NIR), which makes them ideal candidates for NIR-to-NIR-DC bioimaging applications.[30,31]

Interestingly, it has also been reported that the UCL and DCL emission processes depend on the size of $NaYF_4$:Yb^{3+},Er^{3+} nanoparticles. The UCL intensity increases as the size of nanoparticles increases, whereas in DCL, the most efficient emission occurs for diameters ranging from 15 nm to 40 nm when high excitation intensities are used.[32] Similarly, DCL and UCL might show different Yb^{3+}/Er^{3+} doping ratio dependence since different energy levels are involved in the upconversion and downconversion emission processes. Therefore, understanding the NIR-DCL dependence with doping ratios is still needed for optimizing the use of UCNPs in bioimaging applications. Only a few studies deal with the effect of the doping ratio on the upconversion and downconversion emission processes using broader variations in concentrations of the dopants and even less analyzing the emission properties above and below the saturation excitation intensity.

Our aim in this work was to test the robustness of the optimal concentrations of Er^{3+} and Yb^{3+} ions that lead to the highest UCL and DCL. To isolate the effect of ion concentration we synthesized monodisperse $NaYF_4$:Yb^{3+},Er^{3+} nanoparticles with identical sizes (30 nm), the same morphological properties (β-phase), and equal total amount of dopants in the matrix. We fixed the sum of the concentration of Yb^{3+} and Er^{3+} dopant ions at 22%, in relation to the total ion concentration (Y^{3+} + Yb^{3+} + Er^{3+} = 100%) while testing different Yb^{3+}/Er^{3+} ratios ranging from the extreme case where only Er^{3+} ions are present to ratio 10. We evaluated the composition and the excitation intensity influence on the upconversion and downconversion processes within these broad ratios range while keeping the total amount of dopants in the matrix constant. A rate equation analysis was performed to reproduce the experimental findings. This theoretical analysis allowed us to study the role of different mechanisms involved in both UCL and DCL processes as the ion dopant concentration was changed.

2 Experimental section

2.1 Chemicals

Ytterbium(III) chloride hexahydrate (99.9%) ($YbCl_3 \cdot 6H_2O$), yttrium(III) chloride hexahydrate (99.9%) ($YCl_3 \cdot 6H_2O$), erbium(III) chloride hexahydrate (99.9%) ($ErCl_3 \cdot 6H_2O$), sodium hydroxide (NaOH) ($\geq$98%), ammonium fluoride (NH_4F) ($\geq$98%), oleic acid (OA) ($\geq$90% GC), 1-octadecene (ODE) (technical grade 90%), methanol (MeOH) ($\geq$99.9% HPLC), ethanol absolute (EtOH), and n-hexane ($\geq$97% GC). All the reagents were purchased from Sigma-Aldrich and used as received.

2.2 Synthesis of $NaYF_4$:Yb^{3+},Er^{3+} UCNPs

Monodisperse β-$NaYF_4$:Yb_x,Er_y nanoparticles with different dopant ratios were synthesized following the thermal co-precipitation method.[33] First, yttrium(III) chloride hexahydrate (236.63 mg, 0.78 mmol), ytterbium(III) chloride hexahydrate, and erbium(III) chloride hexahydrate were dissolved in 1 mL of MeOH. Afterwards, the rare earth methanol solution was mixed with 1-octadecene (15 mL, 46.9 mmol) and oleic acid (6 mL, 19 mmol)

This journal is © The Royal Society of Chemistry 2021

J. Mater. Chem. C, 2021, 9, 8902–8911 | 8903

in a three-neck round bottom flask by moderate stirring. The resultant mixture was heated to 140 °C under a nitrogen flow at a heating rate of 5 °C min^{-1} with a heating mantle (Nahita Blue, Serie 656) coupled to a temperature controller (JP selecta). At this point, traces of HCl and solvents were removed by using a vacuum pump over 20 min. The next step was to add 10 mL of methanol solution containing NaOH (100 mg, 2.5 mmol) and NH$_4$F (148.16 mg, 4.0 mmol), allowing the reaction to incubate for 30 minutes. The temperature was increased again to 110 °C with a heating rate of 4 °C min^{-1} under a N$_2$ flow. Again, a vacuum pump was used over 20 min. Finally, the solution was heated until it reached a temperature of 316 °C and refluxed for 1 h.

After the solution was cooled down to room temperature, nanoparticles were purified by splitting the product into four centrifuge tubes and vigorously mixing them with 4 mL of MeOH. Subsequently, the phases were allowed to separate, and the methanol phase was removed. Then, the sample was centrifuged at 8500 rpm for 20 minutes. The pellet was washed twice with 1 mL of EtOH without redispersing it. The pellet was finally dried and dispersed in 4 mL of hexane for storage. Table 1 shows the different Yb^{3+}/Er^{3+} dopant ratios synthesized in this work.

2.3 Characterization

2.3.1 Morphological characterization. The chemical and morphological characterization of UCNPs was carried out using a JEOL JEM 1010 electron transmission microscope (TEM) working at a voltage of 80 kV. High-resolution images were taken (HR-TEM) using a microscope JEOL JEM 2100 at a working voltage of 200 kV. High-angle annular dark-field (HAADF) scanning TEM and EDX mappings have been realized using an FEI Talos F200X (FEI, USA, 80 kV) coupled to an EDX detector. All samples were prepared by adding 10 µL of the UCNPs solution (*ca.* 3 mg mL^{-1}) on a Cu grid and allowing the solvent to evaporate at room temperature. To determine the crystalline phase, X-ray diffraction (XRD) patterns of the dried UCNP powders were recorded using a PANalytical Model XPPert PRO MPD Multi-Purpose Diffractometer.

2.3.2 Optical characterization. The luminescent emission spectra of UCNPs were measured using a fluorescence home-built system described previously[34] (see the scheme in Fig. 2A). Briefly, the beam from a 976 nm pigtailed 10 W CW excitation

laser (JDSU, L4-9897603) provided with a current and temperature controller (ILX Lightwave, LDX-36025-12, and LDT-5525B, respectively) is transmitted through a long-pass dichroic filter (Semrock, FF757-Di01) and then focused on a micro-cuvette (Hellma 101.015-QS, 3 mm optical path) with a 10× objective. The luminescence coming from the sample is reflected by the dichroic mirror towards a short-pass filter, which blocks the reflected and scattered radiation and works between 770 nm and 1050 nm (Semrock, FF01-775/SP). The beam is then focused into an optical fiber connected to a monochromator (Horiba Jobin Yvon, iHR320). The monochromator uses an 1800 g per mm grating blazed at 500 nm and a photomultiplier tube (Hamamatsu, R928) to measure upconversion luminescence in the green (520–570 nm) and red (640–660 nm) emission bands of UCNPs. IR down conversion spectra (1525–1575 nm) is measured using an InGaAs solid-state detector (Horiba Jobin Yvon, DSS-IGA020TC) and a 900 g per mm grating blazed at 1.5 µm. Different samples were synthesized for each Yb/Er ratio. At least three spectra were collected for each sample. Then, we computed the average intensity of the spectra integrated area within the green, red, or IR emission bands for each ratio and we took the maximum deviation as the error. Results presented without error bars correspond to a single representative measurement.

To characterize the laser intensity at the sample, we measured the laser power using a thermal sensor power meter (Thorlabs, S310C) and the beam size using the slit-scan technique; this size being around 250 µm (full-width at half maximum).

Luminescence lifetimes were measured using the time-resolved photon counting method. The current laser controller generates 40 µs light excitation pulses with a repetition rate of 125 Hz. The Hamamatsu R928 photomultiplier tube that collects the luminescence signal is connected to a 50 ohm input of a digital oscilloscope (Agilent, DSO9104A). The signal from the current laser controller is used to trigger the oscilloscope. A program (developed in Matlab) is used to analyze each signal directly obtained in real-time on the oscilloscope, and this code can simulate the discriminator and the multichannel counter. Upon analysis of more than 5000 trigger signals, we obtain a luminescence decay curve. The luminescence lifetime was obtained by fitting decay curves to a single exponential function. For the fitting, we considered a time window from t_{ini} to t_{end}, where the final fitting time t_{end} was set long enough to allow the complete decay of luminescence (around t_{end} = 2 ms). For each experimental decay curve, we calculated around 25 fits by changing the initial fitting time t_{ini} within the range where the luminescence signal intensity varies from 70% to 30% of its maximum value. This fitting procedure gives us an average lifetime with its standard error.

3 Results and discussion

The emission properties of NaYF$_4$:Yb,Er nanoparticles are highly dependent on their size, crystalline phase, dopant ion distribution, surface ligand, and surrounding medium, as well

Table 1 Relation between the number of moles of dopants used. In all cases, the number of moles of Y^{3+} remained constant at 0.78 mmol where 100% corresponds to the sum of the moles of Y^{3+}, Yb^{3+}, and Er^{3+} ions

Ratio Yb^{3+}/Er^{3+}	Yb^{3+} (mmol)	Yb^{3+} (%)	Er^{3+} (mmol)	Er^{3+} (%)
10	0.200	20.0	0.020	2.0
8	0.196	19.6	0.024	2.4
4	0.176	17.6	0.044	4.4
1	0.110	11.0	0.110	11.0
0.25	0.044	4.4	0.176	17.6
0.12	0.024	2.4	0.196	19.6
0.1	0.020	2.0	0.200	20.0
0	0	0	0.220	22.0

8904 | *J. Mater. Chem. C*, 2021, **9**, 8902–8911

This journal is © The Royal Society of Chemistry 2021

as on their dopant ion composition. To isolate the effect of the dopant concentration properly, we need to keep other factors affecting luminescence constant. Thus, we have synthesized monodispersed β-NaYF$_4$:Yb$_x$,Er$_y$ nanoparticles with a total codoping concentration of 22% ($x + y = 0.22$), and we varied the ratio between Yb^{3+} and Er^{3+} ions (x/y) from 0 to 10 (see Table 1). Some representative ratios have been corroborated from EDS measurements and are included in Fig. S1 (see the ESI†). These nanoparticles have a mean size diameter of 30 ± 2 nm independent on the dopant concentration as observed from TEM images (Fig. 1A, E, I and Fig. S2 in the ESI† where TEM images for all ratios have been included for completeness). HR-TEM images (Fig. 1B, F, and J) obtained from nanoparticles reveal their high crystallinity. In fact, the crystal lattice fringe with a spacing value of d = 0.524 nm, which corresponds to the (100) crystal planes of β-NaYF$_4$, is obtained. Fig. S3 (see the ESI†) depicts the XRD diffraction pattern of the synthesized nanoparticles, showing that hexagonal β-phase reflections are obtained for all of them. Another factor affecting luminescence that should be controlled is the ion distribution. Under some conditions, the different ion reactivity can induce an anisotropic distribution of the ions as previously published.[35] This result leads us to investigate the dopant distribution within nanoparticles using elemental mapping analyses. Fig. 1C, G, and K and the elemental profile analysis shown in Fig. 1D, H, and L prove that there are no appreciable changes in the distribution of ions within the particles for different Yb/Er ratios. Finally, luminescence surface quenching in oleate-coated UCNPs dispersed in hexane is mainly ascribed to low energy vibrational modes of the CH-groups that bridge the energy gap from the green- and red-emitting levels to the next lower energy level (2800–3000 cm^{-1}). This effect is much weaker than that in non-organic polar solvents, such as water, where higher energy vibrational modes of OH-groups (3200–3600 cm^{-1}) deactivate in a more efficient way at the IR excitation level of Yb^{3+} ions and consequently Er^{3+} ions.[36–38] Considering that as Er^{3+} ions are uniformly distributed in the NP, the percentage of Er^{3+} ions located within its outermost shell (with respect to the total Er^{3+} ions in the NP) will remain constant when increasing the Yb/Er ratio, so it is reasonable to consider that the surface luminescence quenching should not play a relevant role in the observed dependence of luminescence on the Yb/Er ratio.

This information highlights the absence of morphological and structural variations among the different synthesized nanoparticles, and rules out the possible ligand–solvent luminescence variations due to dopant concentrations. Therefore, the photoluminescence variations are mostly due to the presence of different concentrations of dopants ions.
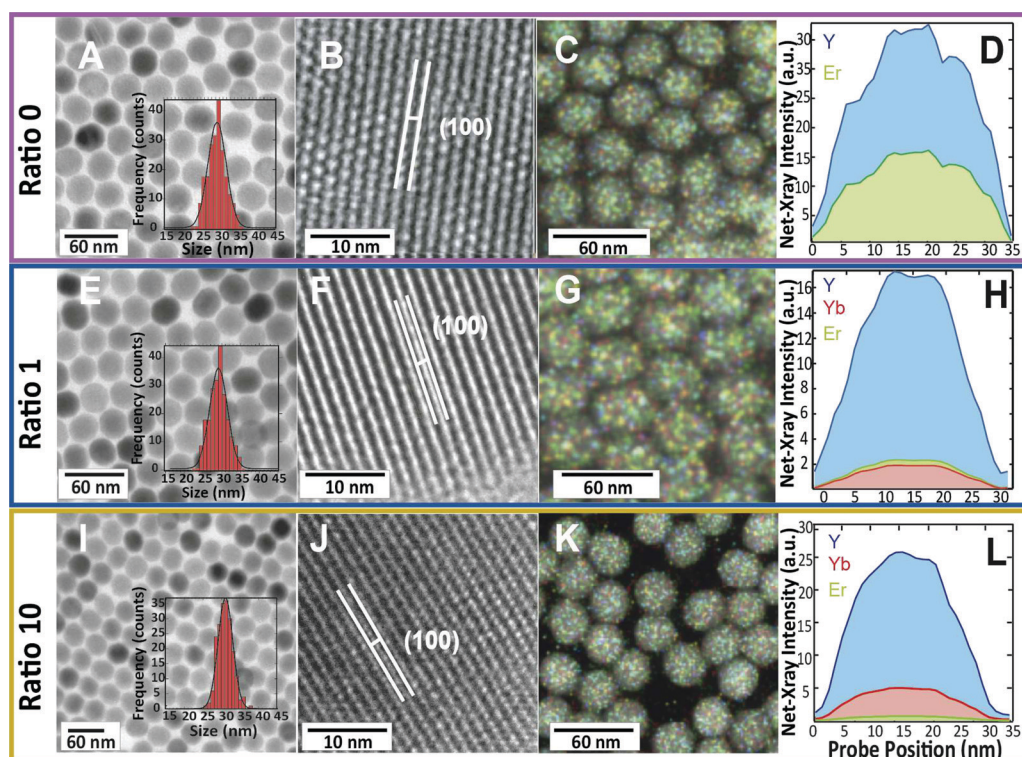
Fig. 1 TEM micrographs of the synthesized nanoparticles (A, E, and I); the inset in each figure shows the size distribution of nanoparticles. A detailed crystalline nanoparticle structure shows the lattice fringe (100) obtained by HR-TEM (B, F, and J). Elemental mapping micrographs of the obtained nanoparticles (C, G, and K). Element distribution profiles of the doping ions within each nanoparticle (D, H, and L). Figures (A–D) correspond to nanoparticles doped with Er^{3+} exclusively (Yb/Er ratio 0). Figures (E–H) correspond to nanoparticles doped with Yb^{3+} and Er^{3+} at a Yb/Er ratio of 1, and figures (I–L) correspond to nanoparticles doped with Yb^{3+} and Er^{3+} at a Yb/Er ratio of 10.

This journal is © The Royal Society of Chemistry 2021

J. Mater. Chem. C, 2021, **9**, 8902–8911 | **8905**

3.1 Luminescence variation with Yb/Er ratio

To analyze the role of Yb/Er ratio on the luminescence properties of UCNPs, we measured, simultaneously, their UCL and DCL spectra under a NIR excitation CW laser at 976 nm. Results presented in Fig. 2C show the spectra obtained from a 1 mg mL^{-1} hexane solution of UCNPs with different Yb/Er ratios excited with an intensity of 5.3 kW cm^{-2}, above the typical saturation value of transition $^2F_{7/2} \rightarrow \,^2F_{5/2}$ of the Yb^{3+} ions, which is $I_{sat}^Y = 3$ kW cm^{-2} (see Section 3.3). Different emission peaks are observed: two green emission peaks near 525 nm and 540 nm corresponding to $^2H_{11/2} \rightarrow \,^4I_{15/2}$ and $^4S_{3/2} \rightarrow \,^4I_{15/2}$ transitions of the Er^{3+} ions, respectively; and a red emission peak around 655 nm corresponding to the $^4F_{9/2} \rightarrow \,^4I_{15/2}$ transition of Er^{3+} ions (see Fig. 2B). Fig. 2C also shows the downconversion luminescence of the NIR peak near 1.55 μm corresponding to the transition from the metastable level of Er^{3+} ions to their ground state, that is, $^4I_{13/2} \rightarrow \,^4I_{15/2}$. In both cases, upconversion and downconversion luminescence emission strongly increases with the Yb/Er ratio. However, above a ratio of 4, no further increase is observed. It should be noted that the range of Er^{3+} and Yb^{3+} concentrations investigated here varies from an Er^{3+} dopant concentration of 22% (ratio 0) where only Er^{3+} ions are present to a well-known standard ratio of 20% of Yb^{3+} and 2% of Er^{3+} (ratio 10). Thus, within this broad dopant range, different photon upconversion mechanisms are expected to occur. Fig. 2B shows different population pathways of UCL emission bands. In the standard case of 20% of Yb^{3+} and 2% of Er^{3+} (ratio 10), the energy transfer from Yb^{3+} ions to Er^{3+} ions should dominate. However, when only Er^{3+} ions are present, the excited-state absorption from the $^4I_{11/2}$ level or the energy transfer between neighboring Er^{3+} ions should be responsible for the UCL emission process. On the other hand, the DCL can be achieved by the ground-state absorption (GSA) of laser photons by both Er^{3+} and Yb^{3+} ions.

To develop more quantitative analysis, we show in Fig. 3A and B the integrated spectra of green and red bands as a function of the Yb/Er ratio for two different excitation intensities, 475 W cm^{-2} below the Yb^{3+} saturation intensity and 5.3 kW cm^{-2} above saturation. Both emission bands show similar behavior, a vast increase in luminescence intensity up to a saturation value reached for Yb/Er ratios above 1 (see the semi-log plot shown in Fig. 3A). A broader variation range (three orders of magnitude difference in luminescence) is observed at low excitation intensities (475 W cm^{-2}) than at high excitation intensities (5.3 kW cm^{-2}), where a two-fold variation range is achieved. This phenomenon can be better visualized in the log–log plot in Fig. 3B. We found that the UCL intensity increases following a power-law behavior with the Yb/Er ratio for ratios below 1. The power-law exponent depends on the excitation intensity. A larger exponent is achieved for the linear absorption regime (below the saturation intensity), which produces the greatest luminescence intensity variation mentioned above.

In Fig. 3C and D, the integrated downconversion spectra are also shown. We observed a similar behavior to that for the upconversion luminescence (see the semi-log plot shown in Fig. 3C). Again, a larger luminescence intensity variation occurs at low laser irradiances, as shown in the log–log plot in Fig. 3D. It should be noted that the power-law exponents found for the DCL are smaller than the ones corresponding to the UCL. Therefore, the upconversion phenomenon is more strongly affected by variations of the Yb/Er ratio than the downconversion luminescence.

In summary, contrary to what is normally assumed, there is not a critical Yb/Er ratio that maximizes the luminescence intensity (usually established as ratio 10), but a wider range of ratios from around 2 to 10 which lead to roughly the same luminescence intensity value. Furthermore, a very slight decrease in the intensity occurs above ratio 4, which corresponds to a fraction of doped ions of 17.6% of Yb^{3+} and 4.4% of Er^{3+}.

As pointed out, the variation of luminescence with an excitation power is greater at low Yb/Er ratios, which could indicate a saturation of luminescence at high Yb/Er ratios. To confirm this, we analyzed the dependence of green and red luminescence with the excitation intensity for the two extreme Yb/Er ratios 10 and 0 (see Fig. 4). For ratio 10 (see circles), a biphotonic process is obtained (power-law exponent close to 2) at excitation intensities below the saturation value of the Yb^{3+} transition. This quadratic behavior points out the nature of the
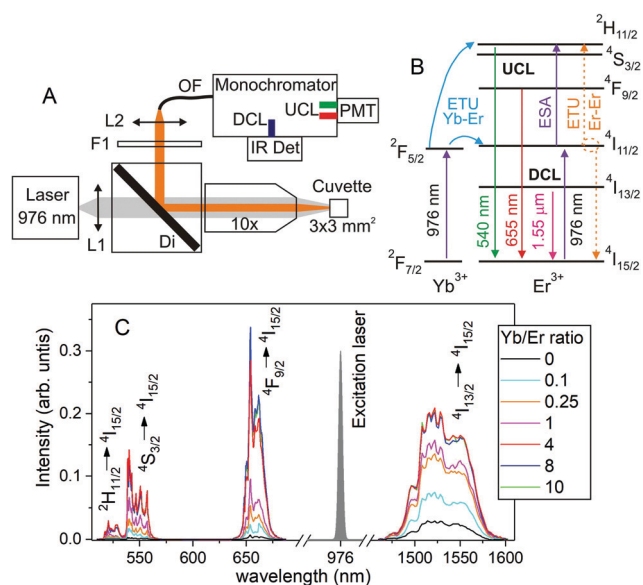
Fig. 2 (A) Scheme for the UCL and DCL detection setup: L1, collimating lens; Di, long-pass dichroic filter; 10×, microscope objective; F1, band-pass filter; L2, focusing lens; OF, optical fiber; PMT, photomultiplier tube; IR Det, infrared detector. (B) The energy level diagram summarizing the biphotonic population pathways of the 520/540 nm green ($^2H_{11/2}$ and $^4S_{3/2} \rightarrow \,^4I_{15/2}$) and 655 nm red ($^4F_{9/2} \rightarrow \,^4I_{15/2}$) emission levels from Er^{3+} ions. The luminescence emission from these levels is represented by solid green and red lines, respectively. A solid pink line represents the radiative downconversion luminescence. Purple lines represent the ground-state absorption for Yb^{3+} and Er^{3+} ions and excited-state absorption for Er^{3+} ions. Blue lines are the energy transfer from Yb^{3+} ions to Er^{3+} ions. Dashed orange lines represent the energy transfer between neighboring Er^{3+} ions. (C) Upconversion and downconversion luminescence spectra for different Yb/Er ratios. Excitation wavelength of 976 nm, and an intensity of 5.3 kW cm^{-2} with a particle concentration of 1 mg mL^{-1}.

8906 | J. Mater. Chem. C, 2021, 9, 8902–8911

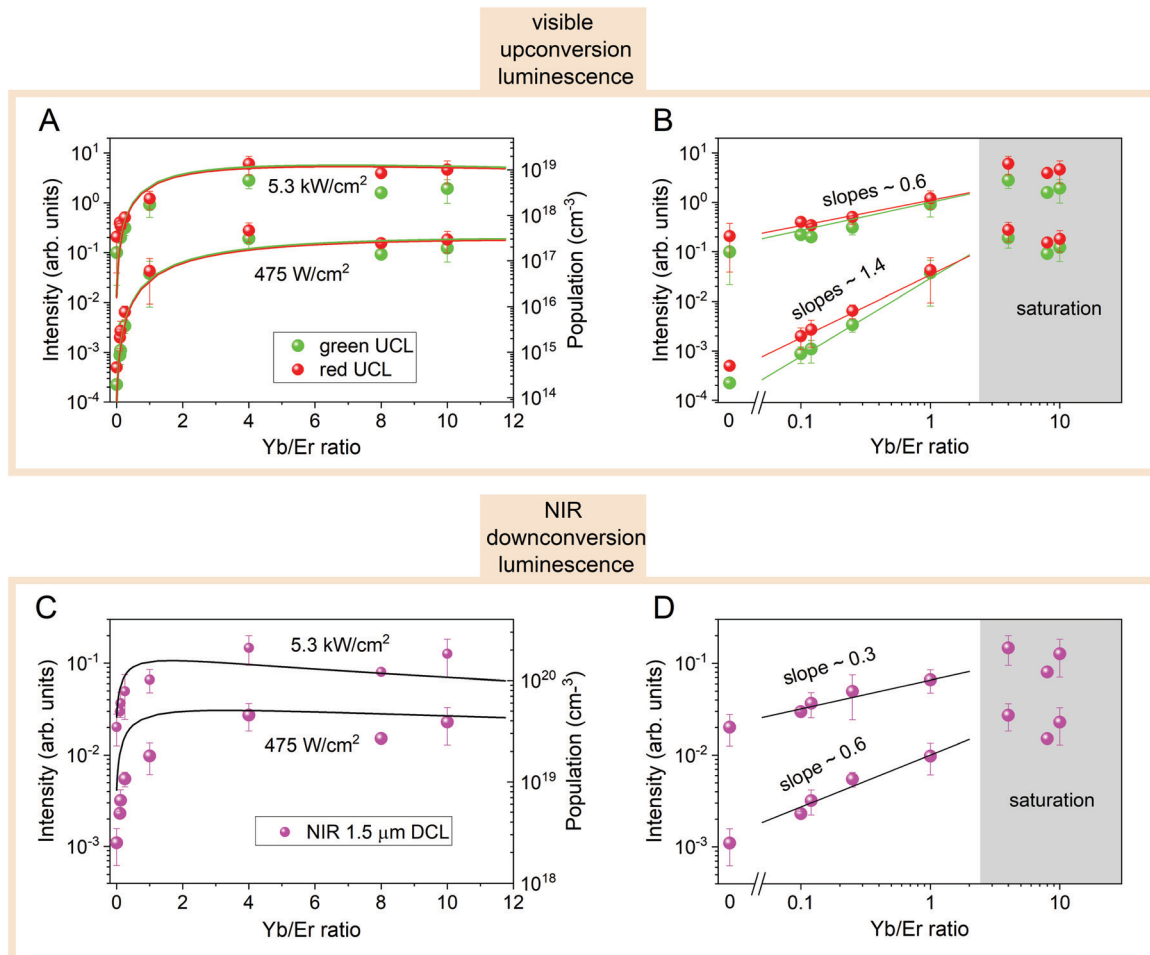This journal is © The Royal Society of Chemistry 2021

Fig. 3 Upconversion (A and B) and downconversion (C and D) integrated luminescence as a function of the Yb/Er ratio for two different excitation intensities, 475 W cm^{-2} below saturation intensity and 5.3 kW cm^{-2} above saturation. Left panels (A and C) show the experimental data in the semi-log plot and the simulated intensity (solid line) from the rate equation model (eqn (1)). Right panels (B and D) show a power-law behavior in a log–log plot and a saturation regime for Yb/Er ratios above 1. Ratio 0 has also been included in the log–log plot. Shadow areas show the ratios at which the luminescence intensity is saturated.
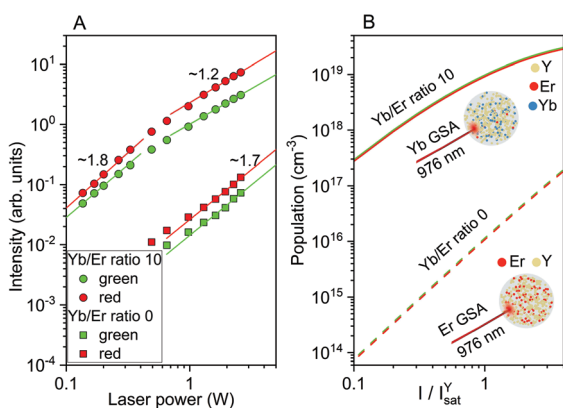

Fig. 4 (A) Green and red upconversion integrated luminescence as a function of the laser power for two extreme Yb/Er ratios: 0 (squares) and 10 (circles). The solid lines are linear fits to the data. (B) Simulated curves: steady-state population of the green and red emission levels as a function of the normalized excitation intensity for the Yb/Er ratio 10 (solid lines) and ratio 0 (dashed lines). UCNP pictures show the proportion of ions for these two Yb/Er ratios indicating, in each case, the ion responsible for the excitation absorption: Yb^{3+} GSA for ratio 10 and Er^{3+} GSA for ratio 0.

underlying upconversion mechanism: two laser photons are needed to obtain a visible emitted photon. However, at excitation intensities above the saturation one, the quadratic behavior saturates due to the absorption saturation of the Yb^{3+} transition leading to an exponent closer to one. For the Yb/Er ratio 0 (see squares), the quadratic behavior (biphotonic process) remains for all excitation powers. In this case, the first step of the UCL emission process is through the ground state absorption of the $^4I_{15/2} \rightarrow \, ^4I_{11/2}$ transition from Er^{3+}. This transition has a larger saturation intensity, which is not reached by the laser power used in the experiments, and therefore, it is still operating in the linear absorption regime.

3.2 Time-resolved luminescence analysis

Let us now analyze the time-resolved UCL for UCNPs with different Yb/Er ratios. Fig. 5 shows the luminescence decay curves at both UCL bands: the green band at 539 nm and the red band at 654 nm. Luminescence signals coming from UCNPs at different ratios roughly match each other, which in principle indicates a negligible influence of the Yb/Er ratio.
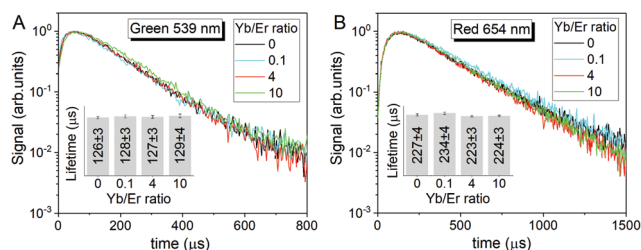
This journal is © The Royal Society of Chemistry 2021

J. Mater. Chem. C, 2021, **9**, 8902–8911 | **8907**

Fig. 5 (A) Green and (B) red upconversion luminescence decay signals for UCNPs with different Yb/Er ratios. (inset) Lifetime values obtained by exponential fitting of decay curves.

We obtained a lifetime of around 127 μs for the green UCL and around 227 μs for the red UCL. Therefore, the Yb/Er ratio does not significantly affect the decay dynamics of the UCL emission process. The results support the idea that the UCL intensity depends on how efficiently are the green- and red-emitting levels populated in terms of the total number of sensitizers (Yb^{3+} ions) and emitters (Er^{3+} ions), and rule out a possible variation of the surface luminescence quenching effect with the Yb/Er ratio. The decay curves in Fig. 5 show an initial increase, that is a signature of the upconversion process by means of the energy transfer from Yb^{3+} to Er^{3+} ions. Interestingly, this initial luminescence increase also appears when decreasing the Yb/Er ratio, even at ratio 0, where only Er^{3+} ions are present. This result indicates that an energy transfer process occurs between neighboring Er^{3+} ions, which will compete with the excited state absorption process.

3.3 Rate equation analysis

Let us theoretically interpret the steady-state luminescence experiments by performing a rate equation analysis. We used the following rate equation model, which describes the main physical mechanism of our system (see details in Fig. 6):

$$\frac{dN_1}{dt} = -W_1 N_1 + W_{21} N_2 - K_3 N_1 N_1^Y$$
$$- \frac{\sigma_{13}}{\sigma_{02}} \frac{W_1 I}{I_{sat}} (N_1 - N_3) - 2C1 N_1^2,$$

$$\frac{dN_2}{dt} = -W_2 N_2 + W_{32} N_3 + K_2 N_0 N_1^Y - K_{B2} N_2 N_0^Y - K_4 N_2 N_1^Y$$
$$+ \frac{W_1 I}{I_{sat}} (N_0 - N_2) - \frac{\sigma_{24}}{\sigma_{02}} \frac{W_1 I}{I_{sat}} N_2 + C_1 N_1^2 - 2C_2 N_2^2,$$

$$\frac{dN_3}{dt} = -W_3 N_3 + W_{43} N_4 + K_3 N_1 N_1^Y + \frac{\sigma_{13}}{\sigma_{02}} \frac{W_1 I}{I_{sat}} (N_1 - N_3),$$

$$\frac{dN_4}{dt} = -W_4 N_4 + K_4 N_2 N_1^Y + \frac{\sigma_{24}}{\sigma_{02}} \frac{W_1 I}{I_{sat}} N_2 + C_2 N_2^2,$$

$$\frac{dN_1^Y}{dt} = -W_1^Y N_1^Y + \frac{W_1^Y I}{2I_{sat}^Y} (N_0^Y - N_1^Y) - K_2 N_0 N_1^Y$$
$$= + K_{B2} N_2 N_0^Y - K_3 N_1 N_1^Y + K_4 N_2 N_1^Y.$$

$$(1)$$

Here N_j is the density of Er^{3+} ions in the energy level j, where the subscripts $j = 0, 1, 2, 3,$ and 4 represent the $^4I_{15/2}$, $^4I_{13/2}$, $^4I_{11/2}$,

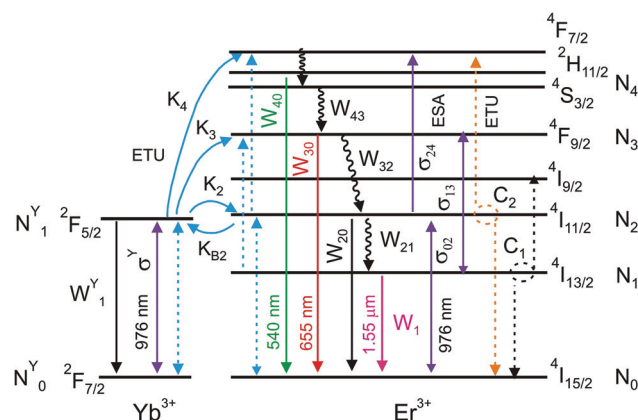**Fig. 6** Energy level diagram for Yb^{3+} and Er^{3+} ions describing the physical processes used in our rate equation model. Blue lines represent the Yb–Er ETU mechanism (K_2, K_{B2}, K_3, K_4), whereas orange and black dashed lines represent different Er–Er ETU mechanisms (C_2 and C_1). Purple lines represent the ground state absorption of Yb^{3+} (σ^Y) and Er^{3+} (σ_{02}) ions and the excited-state absorption of Er^{3+} ions (σ_{13} and σ_{24}). Solid lines represent radiative decay rates from different levels (W_1^Y for Yb^{3+} and W_1, W_{20}, W_{30}, W_{40} for Er^{3+}), whereas faster nonradiative decay rates are represented by wavy lines (W_{43}, W_{32}, and W_{21}).

$^4F_{9/2}$, and $^4S_{3/2}$ energy levels of Er^{3+} ions, respectively (see Fig. 6). The populations of fast-decaying levels as $^4F_{7/2}$ and $^4I_{9/2}$ were neglected and the populations of energy levels $^2H_{11/2}$ and $^4S_{3/2}$ are in thermal equilibrium. N_0^Y and N_1^Y are the Yb^{3+} ion density in the $^2F_{7/2}$ and $^2F_{5/2}$ energy levels. W_{jl} is the decay rate from level j to level l, whereas W_j (W_j^Y for Yb^{3+} ions) is the total decay rate of the energy level j. The decay rates from the excited-level to the ground state were considered as radiative decay rates (in the millisecond range) and corresponding to the next lower level as a faster nonradiative decay (microsecond range) through multi-phonon relaxation. On the other hand, K_2, K_3 and K_4 are the coefficients of the resonant energy transfer from Yb^{3+} ions (sensitizers) to levels 2, 3, and 4 of Er^{3+} ions (activators), respectively. K_{B2} is the coefficient of the back energy transfer from Er^{3+} ions in level 2 to Yb^{3+} ions. C_1 and C_2 are the coefficients of energy transfer between neighboring Er^{3+} ions. C_1 represents a quenching mechanism for erbium-doped amplifiers ($^4I_{13/2}$, $^4I_{13/2}$) → ($^4I_{15/2}$, $^4I_{9/2}$) and C_2 represents an upconversion energy transfer to the green-emitting level ($^4I_{11/2}$, $^4I_{11/2}$) → ($^4I_{15/2}$, $^4F_{7/2}$). σ_{jl} is the absorption ($\simeq$ emission) cross-section at the laser frequency for transition from level j to level l of Er^{3+} ions. The absorption cross-section of the Yb^{3+} transition is σ^Y. The laser intensity is denoted as I (in units of W cm^{-2}) and is normalized to the saturation intensity $I_{sat}^Y = \hbar\omega W_1^Y/(2\sigma^Y)$ for the Yb^{3+} transition and to $I_{sat} = \hbar\omega W_1/\sigma_{02}$ for the Er^{3+} transitions resonant with the excitation laser wavelength at 976 nm, where $\hbar\omega$ is the photon excitation energy.

In our simulations, we considered the decay, energy transfer coefficient, and absorption cross-section values of the same order of magnitude as those found in the literature[26,39–41] (see Section S4 in the ESI†). By numerically solving eqn (1), we obtained the steady-state populations for green (N_4), red (N_3), and IR (N_1) emission levels which are proportional to their

luminescence emission intensities. We plotted the simulated populations (see lines in Fig. 3A and C) as a function of the Yb/Er ratio for a laser intensity below ($I/I_{sat}^Y = 0.1$) and above ($I/I_{sat}^Y = 1.2$) the saturation intensity of the Yb^{3+} transition. These simulated curves showed very good agreement with the experimental results. Furthermore, we theoretically analyzed the biphotonic behavior of the upconversion mechanism for the Yb/Er ratios used in Fig. 4A. Then, we computed the population of green ($^4S_{3/2}$) N_4 and red ($^4F_{9/2}$) N_3 emission levels as a function of the excitation intensity. The results, shown in Fig. 4B, showed the same behavior as the one reported in the experiments. For the Yb/Er ratio 0, the laser always operates in the linear absorption regime since the excitation intensity is below the saturation value of the ground state absorption of the Er^{3+} transition $^4I_{15/2} \rightarrow {}^4I_{11/2}$. Therefore, the quadratic behavior remains. However, for the Yb/Er ratio 10, the laser absorption is due to the ground state absorption of the Yb^{3+} transition $^2F_{7/2} \rightarrow {}^2F_{5/2}$. This transition exhibits a lower saturation value so that it can be reached with the excitation laser intensity used in the experiments, and therefore, a saturation of the quadratic behavior occurs.

3.3.1 Mechanisms for DCL. Finally, we used our theoretical model to analyze the contribution of different mechanisms leading to upconversion and downconversion emission processes as a function of the Yb/Er ratio referred to as r hereafter. To produce both UCL and DCL, Er^{3+} ions need first to be excited into the intermediate level $^4I_{11/2}$. The population of this intermediate level is directly responsible for the DC emission process since $^4I_{13/2}$ is populated through the $^4I_{11/2}$ level. Two possible mechanisms populate the intermediate level: (1) direct excitation by the laser, *i.e.*, GSA of Er^{3+} ions (see Scheme 1 in Fig. 7C) and (2) GSA of Yb^{3+} ions and energy transfer (ET) from the $^2F_{5/2}$ level of Yb^{3+} ions to the $^4I_{11/2}$ level of Er^{3+} ions (see Scheme 2 in Fig. 7C). We analyzed the steady-state population N_1 of the $^4I_{13/2}$ level of Er^{3+} ions (see Fig. 7B) with and without considering ET between Yb^{3+} and Er^{3+} ions. Fig. 7B shows that the NIR emission at 1.55 μm was mainly achieved by way of the ET from Yb^{3+} ions to Er^{3+} ions even for very low values of the Yb/Er ratio. In the extreme case of Yb/Er ratios smaller than 0.01, the only mechanism leading to DCL is the GSA of Er^{3+} ions since the small number of Yb^{3+} ions in UCNPs is not able to efficiently populate the $^4I_{11/2}$ level of Er^{3+} ions. To get a deeper insight, we have obtained an analytical expression for the population of the NIR emission level $^4I_{13/2}$ in the low excitation regime using N_2 from eqn (S2) and N_1^Y from eqn (S3) (see Section S5 in the ESI†):

$$N_1 \approx \frac{W_{21} W_1^Y N_{Yb}}{W_1 W_2} \frac{I}{2I_{sat}^Y} + \frac{W_{21} N_{Er}}{W_2 + K_{B2} N_{Yb}} \frac{I}{I_{sat}}, \quad (2)$$

where the first term of the right hand side comes from Yb GSA and Yb–Er ET and the second one from Er GSA. The combination of both the ground state absorption cross sections and the concentrations of activators and sensitizers decides which ion absorbs NIR radiation more efficiently. A similar contribution of both terms takes place for $N_{Yb}/N_{Er} \approx \sigma_{02}/\sigma^Y = 0.04$. As the ground state absorption cross section of Yb^{3+} ions is more than one order of magnitude larger than the corresponding Er^{3+} ions, even at very

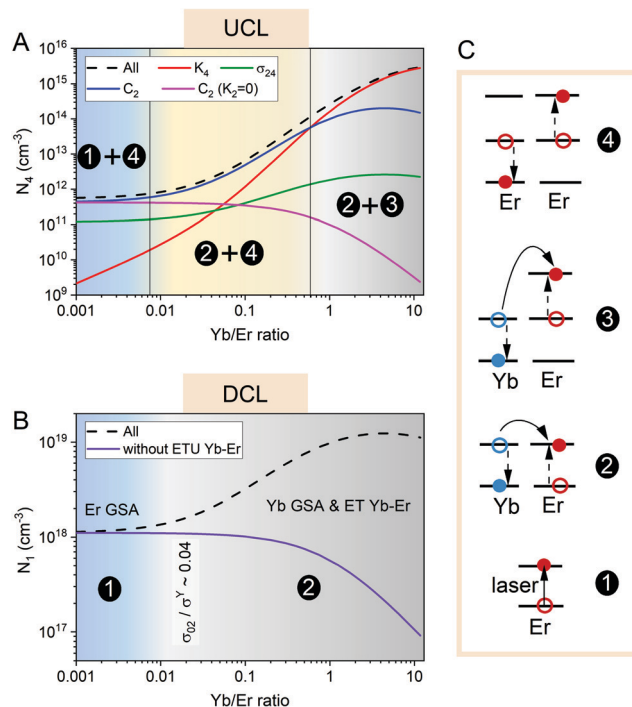**Fig. 7** (A) Steady-state population of the green emission level ($^4S_{3/2}$) N_4 of Er^{3+} ions as a function of the Yb/Er ratio for a laser intensity $I/I_{sat}^Y = 0.01$. Different curves were computed using different pathways that populate the green and red emission levels. (B) Steady-state population of the NIR emission level ($^4I_{13/2}$) N_1 of Er^{3+} ions as a function of the Yb/Er ratio for a laser intensity $I/I_{sat}^Y = 0.01$. Curves were computed with and without accounting for ET between Yb^{3+} and Er^{3+} ions. (C) A schematic of the main mechanisms involved in DCL and UCL.

low Yb/Er ratios, the global absorption can be ascribed to Yb^{3+} ions. Thus, the dependence of the population N_1 on the Yb/Er ratio can be mainly described as proportional to the concentration of Yb^{3+} ions (first term of eqn (2)) which can be written as a function of the Yb/Er ratio, r, as $N_1 \sim N_{Yb} \sim r/(1 + r)$. The behavior given by this simple expression well matches with the power law of the DCL intensity found in the experiments with exponent 0.6. For comparison, Fig. S5 in the ESI† shows the simulated result from eqn (1), the analytical results, and the fit to the experimental data.

3.3.2 Mechanisms for UCL. To produce UCL, once the Er^{3+} ions are excited in the $^4I_{11/2}$ level, three different pathways can populate the green and red emission levels: (1) ETU from the Yb^{3+} ion to the excited Er^{3+} ion (Yb–Er ETU) (see Scheme 3 in Fig. 7C); (2) ESA from this level; (3) ETU from the neighboring excited Er^{3+} ion (Er–Er ETU) (see Scheme 4 in Fig. 7C). Eqn (1) was solved by allowing independently only one of the three possible pathways: (1) Yb–Er ETU controlled by K_4; (2) ESA controlled by σ_{24}; and (3) Er–Er ETU controlled by C_2. Fig. 7A shows the population of the green emission level N_4 as a function of the Yb/Er ratio when only one of the mechanisms is present at a time. For example, the red curve corresponds to Yb–Er ETU and was obtained by setting $\sigma_{24} = 0$ and $C_2 = 0$ in the simulations. We also plotted in the same figure the result obtained when all processes were present (black dashed lines).

This journal is © The Royal Society of Chemistry 2021

J. Mater. Chem. C, 2021, **9**, 8902–8911 | **8909**

We observed how the dominant mechanism of upconversion changes as the Yb/Er ratio varies. At large values of the Yb/Er ratio (above 1), Yb–Er ETU was the dominant mechanism as expected. ET from Yb^{3+} ions to Er^{3+} ions dominates at both steps, first, to populate the intermediate level $^4I_{11/2}$ and then to populate the green emission level (mechanisms 2 and 3 in Fig. 7, respectively). For lower Yb/Er ratios, Yb–Er ETU seems to be negligible since there are very few Yb^{3+} ions to transfer their energy to the excited Er^{3+} ions. Therefore, for Yb/Er ratios below 1, the primary mechanism for obtaining upconversion was the energy transfer between Er^{3+} ions, instead of the ESA process (see Fig. 7A). As we showed in Fig. 7B, the excitation of the intermediate level $^4I_{11/2}$ was due to the ET from Yb^{3+} ions even at values of the Yb/Er ratio as low as 0.01. This means that the population of the green emission level is due to a combination of two types of ET mechanisms: The Yb–Er ET to populate the intermediate level $^4I_{11/2}$ and Er–Er ETU to finally populate the green emission levels (mechanisms 2 and 4 in Fig. 7). We corroborated this by numerically solving eqn (1) considering only Er–Er ETU (using $K_4 = 0$ and $\sigma_{24} = 0$ as we did to obtain the blue line in Fig. 7A) and removing ET processes between Yb^{3+} and Er^{3+} ions that populate the intermediate level ($K_2 = K_{B2} = 0$). In this case (magenta line in Fig. 7A), UCL is produced by GSA of Er^{3+} ions and Er–Er ETU (mechanisms 1 and 4 in Fig. 7). These mechanisms are only relevant for very low values of the Yb/Er ratio when there are virtually no Yb^{3+} ions. In summary, as the Yb/Er ratio was varied, three different mechanisms were found to explain the whole UCL emission process, corresponding to the three different coloured regions shown in Fig. 7A.

We have also obtained an analytical expression for the population of the green emission level valid in the low excitation regime (see eqn (S3) of Section S5 in the ESI†):

$$N_4 \approx \frac{1}{W_4}\left(\frac{W_1^Y}{W_2}\right)^2 N_{Yb}{}^2\left[\frac{K_4}{K_2}\frac{W_2 + K_{B2}N_{Yb}}{N_{Er}} + C_2\right]\left(\frac{I}{2I_{sat}^Y}\right)^2. \quad (3)$$

The first term of the right hand side comes from Yb–Er ETU, which dominates at large Yb/Er ratios. At lower Yb/Er ratios, the second term of eqn (3), which comes from Er–Er ETU, dominates so the population N_4 (and therefore N_3) follows roughly a quadratic dependence on the concentration of Yb^{3+} ions and can be described in terms of the Yb/Er ratio as: $N_4 \sim N_{Yb}{}^2 \sim r^2/(1 + r)^2$. This simple expression gives us the behavior of the UCL intensity with the Yb/Er ratio, being in good agreement with the power-law behavior found in the experiments with exponent 1.4. For comparison, Fig. S5 in the ESI† shows the simulated result from eqn (1), the analytical results, and the fit to the experimental data.

4 Conclusions

We experimentally and theoretically studied the effect of dopant ion concentrations on the UCL and DCL properties of $NaYF_4$:Yb^{3+},Er^{3+} nanoparticles at different excitation intensities. Our approach carefully excluded all other factors whose variation affects luminescence properties, such as the size, morphology, crystal structure, ion distribution, ligand, and surrounding medium, allowing us to exactly infer the influence of the ratio of Yb^{3+} to Er^{3+} ions on the NP luminescence. In particular, we studied the luminescence emission of 30 nm monodisperse β-$NaYF_4$:Yb^{3+},Er^{3+} nanoparticles with a fixed total amount of dopants in the matrix of 22%, by replacing that 22% of Y^{3+} ions with a variable ratio of Yb^{3+} ions to Er^{3+} ions between 0 and 10. In both cases (UCL and DCL), the luminescence emission increased considerably as the Yb/Er ratio increased. However, for ratios greater than four, no additional increase was noted. Larger variation in UCL and DCL was observed when decreasing the excitation intensity. Time-resolved luminescence analyzed in UCL did not show any appreciable change with dopant ratio, indicating a negligible effect of the dopant ratio on the decay dynamics of the UCL emission process.

Finally, a theoretical model was used to analyze the contribution of different mechanisms involved in UCL and DCL when the dopant ratio was varied. According to the results, we confirmed that the dominant mechanism of UCL varied with the Yb/Er ratio. For very low Yb/Er ratios, the Yb–Er ETU was negligible, and the Er–Er ETU process took precedence even over the ESA. Above ratio 1, as expected, the predominant mechanism was the Yb–Er ETU. In the intermediate region of dopant ratios, both energy transfer mechanisms simultaneously contribute to luminescence in a cooperative way: Yb–Er ET to populate the intermediate level of Er^{3+} ions and Er–Er ETU to populate the green and red emitting levels. The DCL emission process in the NIR at 1550 nm was achieved mainly due to the energy transfer of Yb^{3+} ions to Er^{3+} ions. It can be concluded that there was a competition between the GSAs of both types of ions and their concentrations. However, as the Yb^{3+} ions GSA was one order of magnitude greater than that of the Er^{3+} ions, the overall absorption was attributed to the Yb^{3+} ions, even for the lowest, except 0, analyzed Yb/Er ratio of 0.1. Furthermore, analytical expressions for the green $^4S_{3/2}$, red $^4F_{9/2}$ and IR $^4I_{13/2}$ population levels have been obtained in the linear regime of excitation which allowed us to nicely reproduce the experimental power laws of the DCL and UCL intensities.

Conflicts of interest

There are no conflicts to declare.

Acknowledgements

8910 | J. Mater. Chem. C, 2021, 9, 8902–8911

This journal is © The Royal Society of Chemistry 2021

Notes and references

1 F. Auzel, *Chem. Rev.*, 2004, **104**, 139–174.

2 M. Haase and H. Schäfer, *Angew. Chem., Int. Ed.*, 2011, **50**, 5808–5829.

3 F. Wang, R. Deng, J. Wang, Q. Wang, Y. Han, H. Zhu, X. Chen and X. Liu, *Nat. Mater.*, 2011, **10**, 968–973.

4 D. K. Chatterjee, A. J. Rufaihah and Y. Zhang, *Biomaterials*, 2008, **29**, 937–943.

5 G. Chen, H. Qiu, P. N. Prasad and X. Chen, *Chem. Rev.*, 2014, **114**, 5161–5214.

6 D. Mendez-Gonzalez, M. Laurenti, A. Latorre, A. Somoza, A. Vazquez, A. I. Negredo, E. López-Cabarcos, O. G. Calderón, S. Melle and J. Rubio-Retama, *ACS Appl. Mater. Interfaces*, 2017, **9**, 12272–12281.

7 M. You, J. Zhong, Y. Hong, Z. Duan, M. Lin and F. Xu, *Nanoscale*, 2015, **7**, 4423–4431.

8 M. Schoenauer Sebag, Z. Hu, K. de Oliveira Lima, H. Xiang, P. Gredin, M. Mortier, L. Billot, L. Aigouy and Z. Chen, *ACS Appl. Energy Mater.*, 2018, **1**, 3537–3543.

9 P. Alonso-Cristobal, O. Oton-Fernandez, D. Mendez-Gonzalez, J. F. Díaz, E. Lopez-Cabarcos, I. Barasoain and J. Rubio-Retama, *ACS Appl. Mater. Interfaces*, 2015, **7**, 14992–14999.

10 D. Jaque and F. Vetrone, *Nanoscale*, 2012, **4**, 4301–4326.

11 A. Gnach and A. Bednarkiewicz, *Nano Today*, 2012, **7**, 532–563.

12 G. Chen, C. Yang and P. N. Prasad, *Acc. Chem. Res.*, 2013, **46**, 1474–1486.

13 F. Wang and X. Liu, *Chem. Soc. Rev.*, 2009, **38**, 976–989.

14 J. Suyver, J. Grimm, M. van Veen, D. Biner, K. Krämer and H. Güdel, *J. Lumin.*, 2006, **117**, 1–12.

15 S. Schietinger, L. d. S. Menezes, B. Lauritzen and O. Benson, *Nano Lett.*, 2009, **9**, 2477–2481.

16 D. T. Klier and M. U. Kumke, *J. Mater. Chem. C*, 2015, **3**, 11228–11238.

17 S. Fischer, B. Fröhlich, K. W. Krämer and J. C. Goldschmidt, *J. Phys. Chem. C*, 2014, **118**, 30106–30114.

18 S. Wilhelm, *ACS Nano*, 2017, **11**, 10644–10653.

19 C. T. Xu, Q. Zhan, H. Liu, G. Somesfalean, J. Qian, S. He and S. Andersson-Engels, *Laser Photonics Rev.*, 2013, **7**, 663–697.

20 M. Wang, Y. Tian, F. Zhao, R. Li, W. You, Z. Fang, X. Chen, W. Huang and Q. Ju, *J. Mater. Chem. C*, 2017, **5**, 1537–1543.

21 K. W. Krämer, D. Biner, G. Frei, H. U. Güdel, M. P. Hehlen and S. R. Lüthi, *Chem. Mater.*, 2004, **16**, 1244–1251.

22 C. Renero-Lecuna, R. Martín-Rodríguez, R. Valiente, J. González, F. Rodríguez, K. W. Krämer and H. U. Güdel, *Chem. Mater.*, 2011, **23**, 3442–3448.

23 Y. Wang, R. Deng, X. Xie, L. Huang and X. Liu, *Nanoscale*, 2016, **8**, 6666–6673.

24 S. Wen, J. Zhou, K. Zheng, A. Bednarkiewicz, X. Liu and D. Jin, *Nat. Commun.*, 2018, **9**, 2415.

25 B. Cao, Y. He, L. Zhang and B. Dong, *J. Lumin.*, 2013, **135**, 128–132.

26 M. Kaiser, C. Würth, M. Kraft, T. Soukka and U. Resch-Genger, *Nano Res.*, 2019, **12**, 1871–1879.

27 T. D. Cao, T. G. Le, T. N. Nguyen, T. N. Dau, V. T. Nguyen and T. V. Tran, *J. Mol. Struct.*, 2020, **1210**, 128014.

28 B. Shen, S. Cheng, Y. Gu, D. Ni, Y. Gao, Q. Su, W. Feng and F. Li, *Nanoscale*, 2017, **9**, 1964–1971.

29 C. Ma, X. Xu, F. Wang, Z. Zhou, D. Liu, J. Zhao, M. Guan, C. I. Lang and D. Jin, *Nano Lett.*, 2017, **17**, 2858–2864.

30 M. Kamimura, N. Kanayama, K. Tokuzen, K. Soga and Y. Nagasaki, *Nanoscale*, 2011, **3**, 3705–3713.

31 J. Hu, Y. Zhang, H. Xia, H. Ye, B. Chen and Y. Zhu, *Inorg. Chem.*, 2018, **57**, 7792–7796.

32 X. Chen, Y. Zhu, D. Zhou, W. Xu, J. Zhu, G. Pan, Z. Yin, H. Wang, S. Cui and H. Song, *J. Mater. Chem. C*, 2017, **5**, 2451–2458.

33 M. Lin, Y. Zhao, S. Wang, M. Liu, Z. Duan, Y. Chen, F. Li, F. Xu and T. Lu, *Biotechnol. Adv.*, 2012, **30**, 1551–1561.

34 S. Melle, O. G. Calderón, M. Laurenti, D. Mendez-Gonzalez, A. Egatz-Gómez, E. López-Cabarcos, E. Cabrera-Granado, E. Díaz and J. Rubio-Retama, *J. Phys. Chem. C*, 2018, **122**, 18751–18758.

35 R. Shi, X. Ling, X. Li, L. Zhang, M. Lu, X. Xie, L. Huang and W. Huang, *Nanoscale*, 2017, **9**, 13739–13746.

36 R. Arppe, I. Hyppänen, N. Perälä, R. Peltomaa, M. Kaiser, C. Würth, S. Christ, U. Resch-Genger, M. Schäferling and T. Soukka, *Nanoscale*, 2015, **7**, 11746–11757.

37 C. Würth, M. Kaiser, S. Wilhelm, B. Grauel, T. Hirsch and U. Resch-Genger, *Nanoscale*, 2017, **9**, 4283–4294.

38 F. T. Rabouw, P. T. Prins, P. Villanueva-Delgado, M. Castelijns, R. G. Geitenbeek and A. Meijerink, *ACS Nano*, 2018, **12**, 4812–4823.

39 R. B. Anderson, S. J. Smith, P. S. May and M. T. Berry, *J. Phys. Chem. Lett.*, 2014, **5**, 36–42.

40 N. U. Wetter, A. M. Deana, I. M. Ranieri, L. Gomes and S. L. Baldochi, *IEEE J. Quantum Electron.*, 2010, **46**, 99–104.

41 S. Fischer, H. Steinkemper, P. Löper, M. Hermle and J. C. Goldschmidt, *J. Appl. Phys.*, 2012, **111**, 013109.

This journal is © The Royal Society of Chemistry 2021

J. Mater. Chem. C, 2021, **9**, 8902–8911 | **8911**